



**Magnetic and vibronic terahertz excitations in Zn-doped  $\text{Fe}_2\text{Mo}_3\text{O}_8$** B. Csizi <sup>1</sup>, S. Reschke,<sup>1</sup> A. Strinić,<sup>1</sup> L. Prodan <sup>1,2</sup>, V. Tsurkan,<sup>1,2</sup> I. Kézsmárki,<sup>1</sup> and J. Deisenhofer<sup>1</sup><sup>1</sup>*Experimentalphysik V, Center for Electronic Correlations and Magnetism, Institute for Physics,**Augsburg University, D-86135 Augsburg, Germany*<sup>2</sup>*Institute of Applied Physics, MD-2028 Chişinău, Republic of Moldova*

(Received 24 March 2020; revised 5 October 2020; accepted 22 October 2020; published 5 November 2020)

We report on optical excitations in the magnetically ordered phases of multiferroic  $\text{Fe}_{1.86}\text{Zn}_{0.14}\text{Mo}_3\text{O}_8$  in the frequency range  $10\text{--}130\text{ cm}^{-1}$  ( $0.3\text{--}3.9\text{ THz}$ ). In the collinear easy-axis antiferromagnetic phase below  $T_N = 50\text{ K}$ , 11 optically active modes have been observed in finite magnetic fields, assuming that the lowest-lying mode is doubly degenerate. The large number of modes reflects either a more complex magnetic structure than in pure  $\text{Fe}_2\text{Mo}_3\text{O}_8$  or that spin-stretching modes become active in addition to the usual spin precessional modes. Their magnetic field dependence, for fields applied along the easy axis, reflects the irreversible magnetic-field-driven phase transition from the antiferromagnetic ground state to a ferrimagnetic state, while the number of modes remains unchanged in the covered frequency region. We determined selection rules for some of the antiferromagnetic modes by investigating all polarization configurations and identified magnetic- and electric-dipole active modes as well. In addition to these sharp resonances, a broad electric-dipole active excitation band, which is not influenced by the external magnetic field, occurs below  $T_N$  with an onset at  $12\text{ cm}^{-1}$ . We are able to model this absorption band as a vibronic excitation related to the lowest-lying  $\text{Fe}^{2+}$  electronic states in a tetrahedral environment.

DOI: [10.1103/PhysRevB.102.174407](https://doi.org/10.1103/PhysRevB.102.174407)**I. INTRODUCTION**

Multiferroic compounds have been a focus of condensed-matter research for the past two decades [1,2] and, more recently, have attracted interest due to the possible dynamic magnetoelectric effects, such as, for example, unidirectional light propagation [3] and potential applications in spintronics based on antiferromagnetic materials [4,5].

The multiferroic compound  $\text{Fe}_2\text{Mo}_3\text{O}_8$ , which is known as the mineral kamiokite [6], adopts a hexagonal unit cell with lattice constants  $a = 5.777\text{ Å}$  and  $c = 10.057\text{ Å}$  at room temperature as depicted in Fig. 1(a) [7]. It belongs to the polar space group  $P6_3mc$  with a polarization along the  $c$  axis [8,9]. The  $\text{Fe}^{2+}$  ions occupy two different sites with tetrahedral (site A) and octahedral oxygen coordination (site B) [10]. The two types of corner-sharing polyhedra form honeycomblike layers in the  $ab$  plane separated by breathing kagome layers of molybdenum octahedra as shown in Fig. 1(b). The Mo layers do not contribute to the magnetism due to spin-singlet formation of structural  $\text{Mo}_3\text{O}_{13}$  clusters [11,12].  $\text{Fe}_2\text{Mo}_3\text{O}_8$  exhibits a collinear antiferromagnetic (AFM) order of the iron ions below the Néel temperature  $T_N = 60\text{ K}$ , which is accompanied by a strong increase of the polarization [10,13], giving rise to a type-I multiferroic state and strong magneto-optical effects [14–16]. In addition, an applied magnetic field along the  $c$  axis induces a ferrimagnetic (FiM) order [10,13]. Recently, the possibility of additional orbital ordering on the Fe sites in both the AFM and the FiM state has been suggested by *ab initio* calculations [17].

Isovalent substitution of Fe by nonmagnetic Zn in  $(\text{Fe}_{1-y}\text{Zn}_y)_2\text{Mo}_3\text{O}_8$  has been reported to influence the mag-

netic phase diagram, leading to a stabilization of the ferrimagnetic phase with increasing Zn content [13,18]. Previous studies have revealed that the  $\text{Zn}^{2+}$  ions predominantly occupy the tetrahedral sites for  $y \leq 0.5$  [11,19]. Both the antiferromagnetic and the ferrimagnetic phases of  $(\text{Fe}_{1-y}\text{Zn}_y)_2\text{Mo}_3\text{O}_8$  reportedly exhibit interesting electric- and magnetic-dipole active magnon excitations and, furthermore, intricate magneto-optical effects, e.g., gyrotropic birefringence [15] and the optical diode effect [16]. In this study we investigated the low-energy excitations in single crystals of  $\text{Fe}_{1.86}\text{Zn}_{0.14}\text{Mo}_3\text{O}_8$  by terahertz (THz) spectroscopy. At this Zn concentration we have the possibility to study the dynamic fingerprints of the magnetic-field-induced transition regime and both phases in a suitable magnetic field range: For  $y = 0.05$  the FiM phase for  $T < 30\text{ K}$  can only be reached for  $H > 5\text{ T}$ , and for  $y = 0.125$  the antiferromagnetic phase reportedly occurs only as a metastable state [13]. Moreover, magnetic-field-dependent THz measurements in Faraday configurations have not been reported previously for  $y = 0$  or  $y = 0.125$  [14], making a value of  $0.05 < y < 0.125$  a suitable concentration to shed light on the dynamical properties of both phases in a detailed THz transmission study.

**II. EXPERIMENTAL DETAILS**

Polycrystalline  $(\text{Fe}_{1-y}\text{Zn}_y)_2\text{Mo}_3\text{O}_8$  samples were prepared by repeated synthesis at  $1000^\circ\text{C}$  of binary oxides FeO (99.999%),  $\text{MoO}_2$  (99%), and ZnO in evacuated quartz ampoules aiming for a concentration with  $x = 0.1$ . Single crystals were grown by the chemical transport reaction method at temperatures between  $950$  and  $900^\circ\text{C}$ .  $\text{TeCl}_4$  was used as

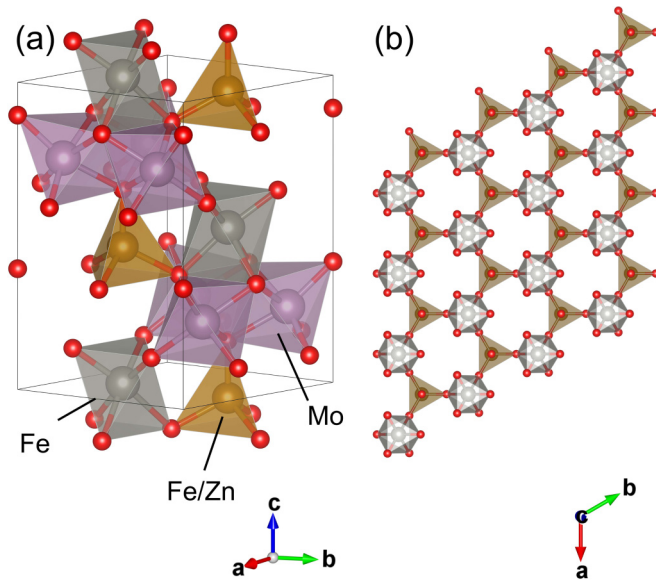


FIG. 1. (a) Double unit cell of  $(\text{Fe}_{1-y}\text{Zn}_y)_2\text{Mo}_3\text{O}_8$ . (b) Top view of the honeycomblike layers stacked along the  $c$  axis.

the source of the transport agent. Large single crystals up to 5 mm were obtained after 4 weeks of transport. The x-ray diffraction pattern of the crushed single crystals shown in Fig. 2(a) revealed a single-phase composition with a hexagonal symmetry using space group  $P6_3mc$  and a Zn content corresponding to  $x \approx 0.07$ . The obtained lattice constants are  $a = b = 5.773(2)$  Å and  $c = 10.017(2)$  Å.

The specific heat was measured in a Quantum Design physical properties measurement system from 1.8 to 300 K and in fields up to 9 T. Magnetization measurements were performed using a superconducting quantum interference device magnetometer (Quantum Design MPMS-5).

Transmission measurements in the frequency range 10–130  $\text{cm}^{-1}$  were performed by THz time-domain spectroscopy using a Toptica TeraFlash spectrometer and an Oxford Instruments Spectromag cryomagnet in external magnetic fields ranging from  $-7$  to 7 T in an  $ac$ -cut sample with a thickness of  $d = 1.48$  mm and an  $ab$ -cut sample with  $d = 0.6$  mm.

### III. SAMPLE CHARACTERIZATION AND PHASE DIAGRAM

The temperature dependence of the specific heat shown in Fig. 2(b) reveals a clear  $\lambda$ -like anomaly at the magnetic ordering transition  $T_N = 50$  K, similar to the reported anomaly of pure  $\text{Fe}_2\text{Mo}_3\text{O}_8$  [10]. With an increasing external magnetic field applied along the crystallographic  $c$  axis the anomaly broadens and shifts to higher temperatures. The transition temperatures were estimated using the maxima of the specific heat.

The temperature dependence of the magnetic susceptibility measured in 1 T shown in Fig. 3(a) exhibits a steep increase and a subsequent maximum at the same temperature as the  $\lambda$  anomaly in the specific heat at  $T_N = 50$  K, confirming that the transition corresponds to the magnetic ordering transition in agreement with previous studies [7,9,13].

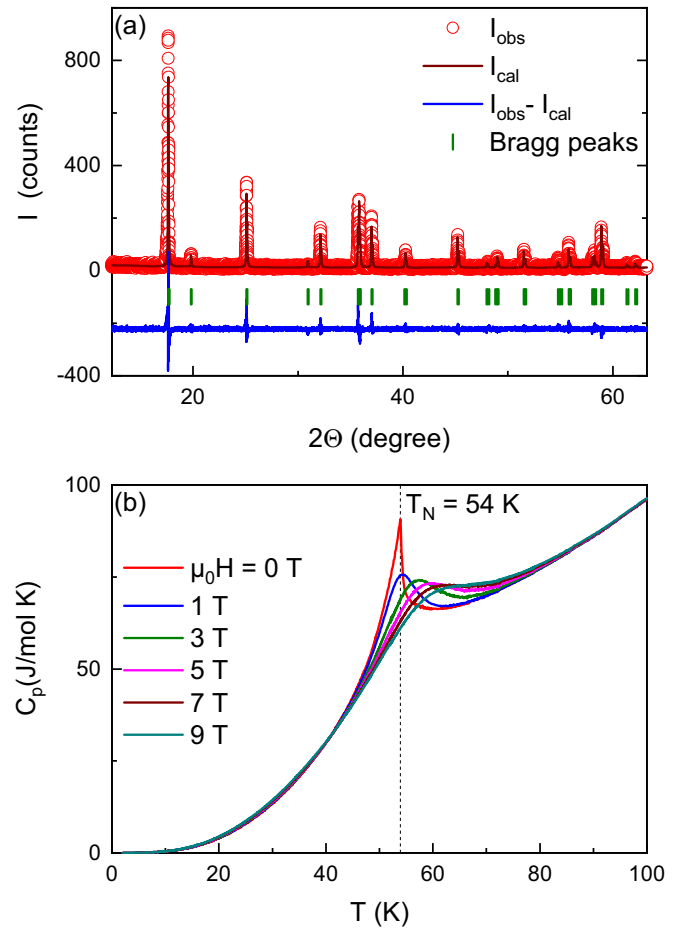


FIG. 2. (a) Room-temperature x-ray diffraction spectra of  $\text{Fe}_{1.86}\text{Zn}_{0.14}\text{Mo}_3\text{O}_8$  and the corresponding calculated pattern for space group  $P6_3mc$ . (b) Temperature-dependent specific heat  $C_p$  in the vicinity of the magnetic ordering transition in magnetic fields applied along the  $c$  axis between 0 and 9 T.

The temperature dependence of  $1/\chi$  in the paramagnetic state range of 100–300 K can be described by a Curie-Weiss law yielding  $\Theta_{\text{CW}} = -40$  K and an effective moment  $\mu_{\text{eff}} = 5.5 \mu_B$ , which is enhanced in comparison to the spin-only value of  $\mu_{\text{eff}} = 4.9 \mu_B$  expected for  $\text{Fe}^{2+}$  ions with spin  $S = 2$ , assuming that all Zn ions occupy tetrahedral sites and that the effective  $g$  factors are 2.1 [20] and 2.0 [21] for the tetrahedral and octahedral Fe sites, respectively. The effective magnetic moment is comparable to reported values of  $\mu_{\text{eff}} = 5.7 \mu_B$  for pure  $\text{Fe}_2\text{Mo}_3\text{O}_8$  [7]. The enhancement compared to the spin-only value could be due to a sizable orbital contribution [17,22]. The obtained Curie-Weiss temperature is clearly reduced in comparison with the values  $\Theta_{\text{CW}} = -110$  or 100 K reported for  $\text{Fe}_2\text{Mo}_3\text{O}_8$  [7,18], but in line with the reported tendency for increasing Zn substitution, where  $\Theta_{\text{CW}}$  eventually becomes positive [18].

The magnetic field dependence of the magnetization for  $H \parallel c$  is shown for several temperatures below  $T_N$  in Fig. 3(b). At 13 K the transition from the antiferromagnetic to the ferrimagnetic state is taking place via a two-step feature characterized by the critical fields  $H_{c1} = 3$  T and  $H_{c2} = 3.8$  T as indicated in Fig. 3(b). This is in agreement with previous

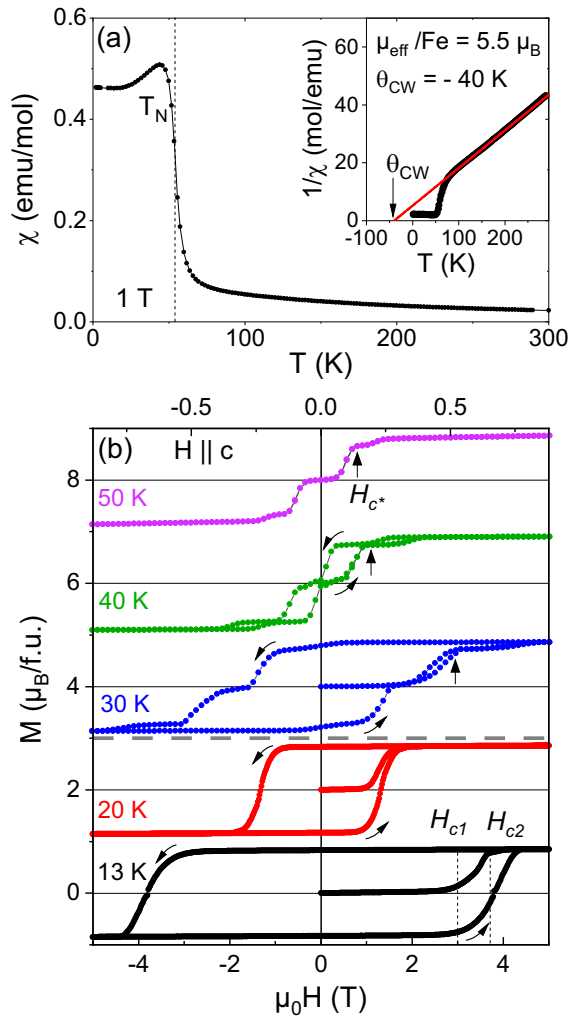


FIG. 3. (a) Temperature dependence of the magnetic susceptibility  $\chi$  measured in 1 T for  $H \parallel c$ . The inset shows the temperature dependence of  $\chi^{-1}$  and a Curie-Weiss fit (solid red line). (b) Field-dependent magnetization curves for several temperatures below  $T_N$ .

studies for samples with  $y = 0.1$  [13]. However, at 50 K, just below the magnetic transition temperature, no hysteretic behavior or formation of a metastable state is observed, but an intermediate third step is observed at  $H_{c^*}$ . At 40 K a hysteretic behavior appears, but the remanent magnetization is still zero, while the width of the hysteresis is clearly increased at 30 K and the remanent magnetization already corresponds to the metastable ferrimagnetic configuration. At 20 K the intermediate step at  $H_{c^*}$  is not discernible anymore and an almost symmetric hysteresis has evolved. In addition, the widths of the hysteretic curves measured by the distance of the coercive fields at 30 and 20 K are 0.27 and 1.3 T, respectively, seem to be enhanced in comparison with the widths shown in Ref. [13] for  $y = 0.1$ . This is in agreement with a less diluted system with a Zn concentration  $y = 0.07$ .

In Fig. 4 the critical fields and temperatures obtained from specific heat and magnetization measurements are summarized in a  $H$ - $T$ -diagram, which can be compared with the phase diagrams for  $y = 0.05$  and  $y = 0.1$  reported by Kuramaji and coworkers [13]. The intermediate magnetization

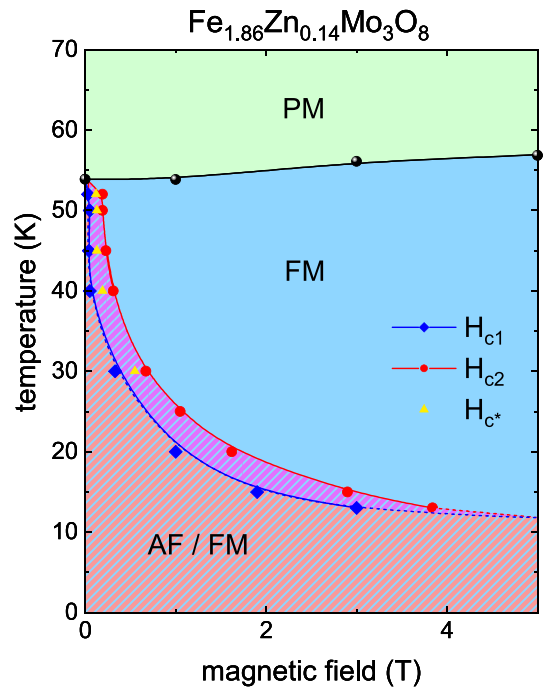


FIG. 4.  $H$ - $T$  phase diagram of  $\text{Fe}_{1.86}\text{Zn}_{0.14}\text{Mo}_3\text{O}_8$  established from specific heat and magnetization measurements. The dashed areas indicate the metastable ferrimagnetic phase as described in the text.

step at  $H_{c^*}$  for temperatures  $T > 20$  K may originate from a more delicate competition between the exchange couplings and the thermal fluctuations at this particular Zn concentration,  $y = 0.07$ . On account of the x-ray diffraction results on crushed single crystals, we discard the possibility that the intermediate steps are due to impurity phases. While for  $y = 0.05$  no remanent magnetization has been reported down to 13 K and the antiferromagnetic ordering appears close to 60 K, for  $y = 0.1$  the metastable state with a finite remanent magnetization appears also in the range 40–30 K and at an ordering temperature similar to that in our case.

## IV. EXPERIMENTAL RESULTS

### A. Temperature-dependent polarized absorption spectra

The temperature dependence of the THz absorption spectra for the polarization configuration  $E^\omega \perp c$ ,  $H^\omega \perp c$  ( $ab$ -cut) and the configurations  $E^\omega \perp c$ ,  $H^\omega \parallel c$  and  $E^\omega \parallel c$ ,  $H^\omega \perp c$  ( $ac$ -cut) are shown in Figs. 5(a)–5(c), respectively. Above  $T_N$ , there are no detectable excitations. The strong monotonous increase in absorption with increasing frequency for  $E^\omega \perp c$  can be attributed to the low-energy tail of the lowest-lying infrared-active phonon of  $E_1$  symmetry with an eigenfrequency of  $130 \text{ cm}^{-1}$  [22,23]. The decreasing absorption of this contribution with decreasing temperature is in agreement with the strong narrowing of the IR-active phonon, when the system is cooled below  $T_N$  [22]. Note that the lowest lying IR-active phonon for  $E^\omega \parallel c$  is located at around  $200 \text{ cm}^{-1}$  [22,23] and, therefore, the frequency range where transmission can be detected is wider than for the  $E^\omega \perp c$  polarization. Upon cooling below  $T_N$ , several new modes emerge or become

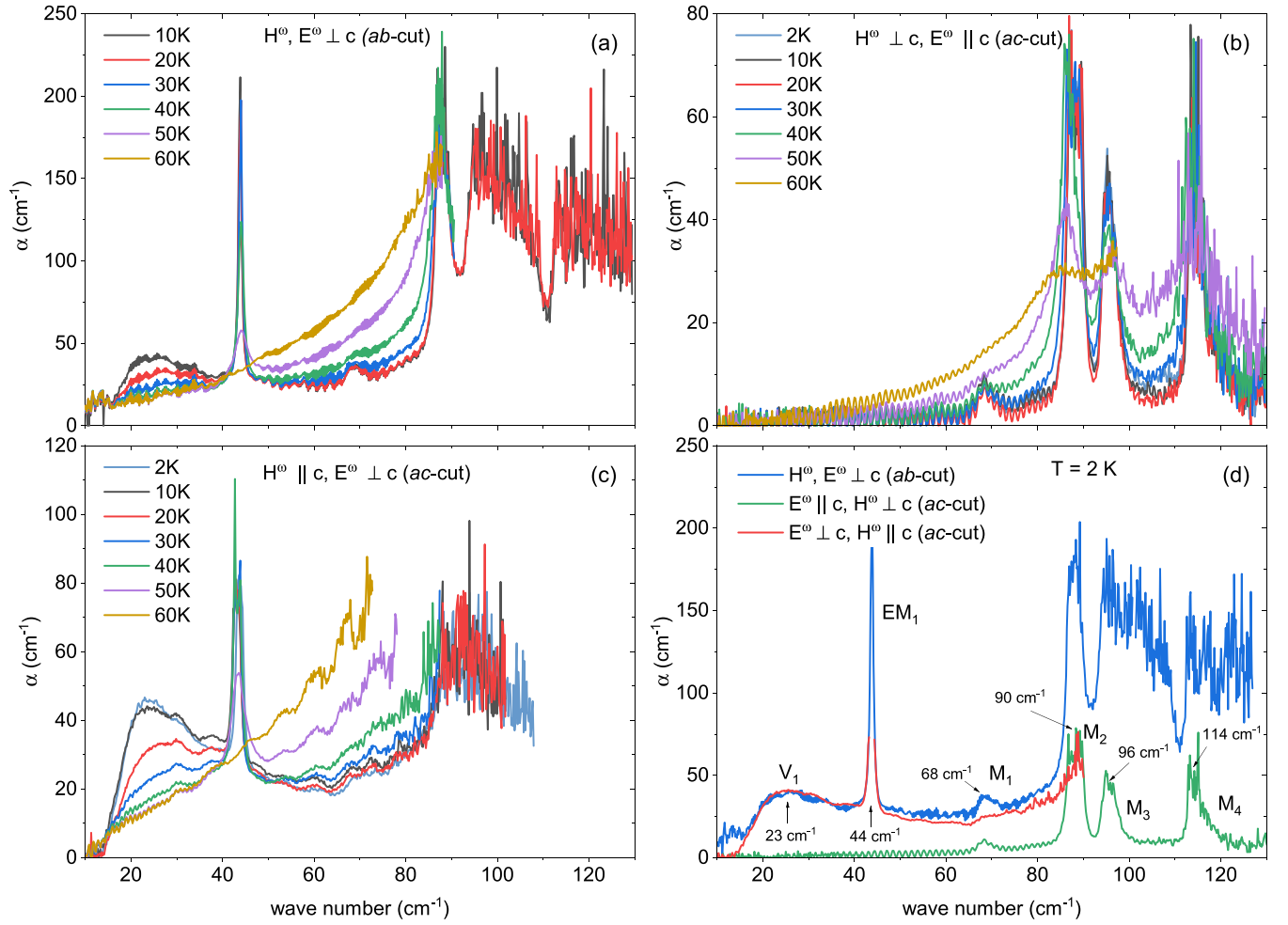


FIG. 5. Absorption spectra for several temperatures above and below  $T_N$  for different polarization configurations: (a)  $E^\omega \perp c, H^\omega \perp c$  (*ab*-cut sample); (b)  $E^\omega \parallel c, H^\omega \perp c$  (*ac*-cut sample), (c)  $E^\omega \perp c, H^\omega \parallel c$  (*ac*-cut sample); and (d) comparison of the absorption spectra at 2 K for the three different configurations.

observable due to the reduced absorption of the IR-phonon contribution in the investigated frequency range. Since all of these modes seem to gain intensity and sharpen upon cooling we assign them to new excitations of the magnetically ordered state.

Note that the high-frequency parts of some spectra are not shown, because the transmission values were too low to give reliable information in this region. For the same reason the absorption maxima of the most intense modes could not be resolved. Whenever this was the case, the eigenfrequency  $\omega_0$  was obtained by assuming a symmetric line shape and choosing the center of the absorption. For the broad band  $V_1$  the frequency of the intensity maximum is given as a characteristic frequency.

A comparison of the spectra measured at 2 K for the three polarization configurations is shown in Fig. 5(d). The resulting selection rules and eigenfrequencies for the detected modes are summarized in Table I together with the modes reported for the AFM phase of pure  $\text{Fe}_2\text{Mo}_3\text{O}_8$  [14]. The lowest-lying broad asymmetric excitation band  $V_1$  and mode  $EM_1$  are observed for the *ab*-cut spectrum as well as in the *ac*-cut spectrum with  $E^\omega \perp c, H^\omega \parallel c$  and are, therefore, assigned to be electric-dipole active for  $E^\omega \perp c$ . The fact that the

intensity of  $V_1$  does not alter for these two configurations implies that it is not magnetic-dipole active. No feature similar to

TABLE I. Upper part: Selection rules for the excitations found in  $\text{Fe}_{1.86}\text{Zn}_{0.14}\text{Mo}_3\text{O}_8$  for the different polarization configurations as shown in Fig. 5. The notation  $\checkmark$  and  $\times$  indicates the presence or absence of a mode. The cases when no observation was possible are denoted as n.r. (not resolved). Lower part: Reported excitations in the AFM phase of pure  $\text{Fe}_2\text{Mo}_3\text{O}_8$  at 4.5 K taken from Ref. [14].

Mode	$\omega_0$ ( $\text{cm}^{-1}$ )	<i>ab</i> -cut		<i>ac</i> -cut		Activity
		$E^\omega \perp c$ $H^\omega \perp c$	$E^\omega \perp c$ $H^\omega \parallel c$	$E^\omega \parallel c$ $H^\omega \perp c$		
$V_1$	23	$\checkmark$	$\checkmark$	$\times$		$E^\omega \perp c$
$EM_1$	44	$\checkmark$	$\checkmark$	$\times$		$E^\omega \perp c$
$M_1$	68	$\checkmark$	$\times$	$\checkmark$		$H^\omega \perp c$
$M_2$	90	$\checkmark$	n.r.	$\checkmark$		$H^\omega \perp c$
$M_3$	96	n.r.	n.r.	$\checkmark$		?
$M_4$	114	n.r.	n.r.	$\checkmark$		?
$EM$	40	$\checkmark$	$\checkmark$	$\times$		$E^\omega \perp c$
$MM_1$	90	$\checkmark$	$\times$	$\checkmark$		$H^\omega \perp c$

the  $V_1$  band has been reported for any other compound of the  $(\text{Fe}_{1-y}\text{Zn}_y)_2\text{Mo}_3\text{O}_8$  series. For  $EM_1$  our data do not allow one to exclude a difference in intensity for the two configurations, because the maximum of  $EM_1$  was not resolved. However, the eigenfrequency and the selection rule for  $EM_1$  are in good agreement with a reported excitation called  $EM$  in pure  $\text{Fe}_2\text{Mo}_3\text{O}_8$  [14] (see Table I), where the intensities for these two configurations seem to show no differences. Therefore, we also discard a possible magnetic-dipole activity of  $EM_1$ . In addition,  $EM_1$  was not observed for a Zn concentration of  $y = 0.125$ , where the AFM phase is completely suppressed and the ground state is ferrimagnetic [14].

In contrast to modes  $V_1$  and  $EM_1$ , the four additional modes,  $M_1$ – $M_4$ , observed at higher frequencies can be excited for  $H^\omega \perp c$  and are thus considered to be magnetic-dipole active. An additional electric-dipole activity is discarded for excitation  $M_1$ , because it does not appear for the configuration  $E^\omega \perp c$ ,  $H^\omega \parallel c$ . For modes  $M_2$ – $M_4$  our spectra for  $E^\omega \perp c$ ,  $H^\omega \parallel c$  do not allow us to unambiguously exclude an electric-dipole activity, but we expect any such contribution to be weak. Note, that a magnetic-dipole active mode (named  $MM_1$ , see Table I) with an eigenfrequency close to  $M_2$  has been reported for  $x = 0$  and  $x = 0.125$ , previously [14], and determined to be only magnetic-dipole active. Modes  $M_1$ ,  $M_3$ , and  $M_4$  have not been observed before, probably due to the low intensity of  $M_1$  and the fact that the frequency range of  $M_3$  and  $M_4$  was not resolved in previous studies.

### B. Magnetic-field-dependent absorption spectra

The magnetic field dependence of the absorption spectra for the three possible polarization configurations measured for  $H \parallel c$  is shown in Figs. 6(a)–6(c). Since the transition to the ferrimagnetic state occurs when the magnetic field is parallel to the  $c$  axis, the  $ab$ -cut sample was measured in the Faraday configuration ( $H \parallel c$ ,  $k \parallel c$ ) and the  $ac$ -cut in the Voigt configuration ( $H \parallel c$ ,  $k \perp c$ ), where  $k$  is the wave vector of the incoming THz beam. Spectra measured with  $H \perp c$  (not shown here) exhibited no field dependence of the absorption spectra.

The measurements were performed at 13 K, where the critical fields  $H_{c1}$  and  $H_{c2}$  of the magnetization steps and the saturation magnetization [see Fig. 3(b)] of the compound were accessible using our experimental setup. When increasing the magnetic field in the antiferromagnetic phase (blue spectra) we observe a linear splitting of the modes  $M_1$ – $M_4$  as indicated by the black lines in Fig. 6(b) in the Voigt configuration and for  $M_1$  also in the Faraday configuration [Fig. 6(c)]. The slope of the linear dependence was parametrized by an effective  $g$  factor defined by  $\hbar\omega = \hbar\omega_0 \pm g_{\text{eff}}\mu_B H$  for both branches. The values are indicated in Figs. 6(e) and 6(f). The behavior of  $M_2$  in the Faraday configuration is more complex, as a low-frequency satellite  $M_5$  seems to emerge and soften with increasing field up to  $H_{c2}$ . For the electric-dipole active mode  $EM_1$ , no shift or splitting with increasing magnetic field could be resolved, but it loses intensity when approaching the transition region to the FiM state and it finally disappears for  $H > H_{c2}$  (spectra for  $H_{c1} < H < H_{c2}$  are shown in green, for  $H > H_{c2}$  in red). This behavior is in agreement with the corresponding  $EM$  mode in pure  $\text{Fe}_2\text{Mo}_3\text{O}_8$  [14]. Above  $H_{c2}$

modes,  $M_1$ – $M_4$  also vanish, and new modes appear in the ferrimagnetic phase. We want to emphasize that the coexistence of modes of the AFM and FiM phases for  $H_{c1} < H < H_{c2}$  indicates a two-phase regime in this field region. These new modes also show a field dependence and are labeled  $F_1$ – $F_{11}$ . A detailed comparison of the splitting of the antiferromagnetic modes at 2 T and the shape of the ferrimagnetic modes at 7 T is given in Fig. 7. Notably, the broad band  $V_1$  does not exhibit any significant changes with increasing magnetic fields and does not seem to be influenced by the transition to the FiM state.

The resonance frequencies of the ferrimagnetic modes  $F_1$ – $F_{11}$  either increase or decrease linearly with increasing magnetic fields as shown in Fig. 6. Additionally, we included the resonance frequencies of modes  $F_1$ – $F_{11}$  measured upon lowering the magnetic field to zero (spectra not shown here) as open symbols in Figs. 6(d)–6(f). The eigenfrequencies of  $F_1$  and  $F_2$  were found to cross each other below  $H_{c1}$ . The eigenfrequencies of  $F_1$ – $F_{11}$  in the zero-field FiM state are given in Table II, together with the effective  $g$  factors. In the lower part of Table II we list all reported modes of the FiM phase of  $(\text{Fe}_{1-y}\text{Zn}_y)_2\text{Mo}_3\text{O}_8$  for a comparison. For  $y = 0$  and  $y = 0.125$  a magnetic-dipole active mode (called  $\nu_3$  or  $MM_2$ ) with an eigenfrequency similar to that of  $F_1$  has been reported [14]. For  $y = 0.25$  and  $y = 0.4$  this mode  $\nu_3$  seems to have developed an additional electric-dipole activity [15]. The additional modes  $\nu_1$ ,  $\nu_2$ , and  $\nu_4$  at lower frequencies cannot be directly related to the modes observed in our study, as we expect a continuous evolution of the modes with increasing Zn content and, therefore, consider the reported spectra for  $y = 0$  and  $y = 0.125$  as the most relevant.

## V. DISCUSSION

### A. Modes $EM_1$ and $M_1$ – $M_5$ of the AFM phase

As already mentioned above, modes  $EM_1$  and  $M_2$  have been reported already for pure  $\text{Fe}_2\text{Mo}_3\text{O}_8$  and interpreted as precessional modes of the collinear AFM structure, both being doubly degenerate modes [14]. While the degeneracy of  $M_2$  is clearly lifted in the external magnetic field with  $g_{\text{eff}} = 1.7$  for  $H^\omega \parallel a$ , the possible doublet nature of  $EM_1$  remains to be confirmed in higher magnetic fields. The respective electric- and magnetic-dipole activity of the two modes were assigned to an inverse Dzyaloshinskii-Moriya mechanism and different single-ion anisotropies of tetrahedral and octahedral sites [14].

As our spectra reveal three additional magnetic modes  $M_1$ ,  $M_3$ , and  $M_4$ , we have to take into account that the disorder induced by substitution of iron by zinc may result in an increased number of nonequivalent tetrahedral Fe sites. In early Mössbauer studies for various zinc dopings at least four different tetrahedral iron sites with different hyperfine fields could be distinguished [11]. Given the absence of  $M_1$  in the spectra of pure  $\text{Fe}_2\text{Mo}_3\text{O}_8$  [14] and the low intensity of the mode, we assume that this mode is due to the Zn-induced disorder. As the spectral range reported for  $\text{Fe}_2\text{Mo}_3\text{O}_8$  was limited to about  $94 \text{ cm}^{-1}$  [14], it is not clear whether  $M_3$  (at  $96 \text{ cm}^{-1}$ ) and  $M_4$  (at  $114 \text{ cm}^{-1}$ ) are also disorder-induced modes or whether they are present in pure  $\text{Fe}_2\text{Mo}_3\text{O}_8$ , too. Preliminary THz measurements on pure  $\text{Fe}_2\text{Mo}_3\text{O}_8$  [24], however, indicate

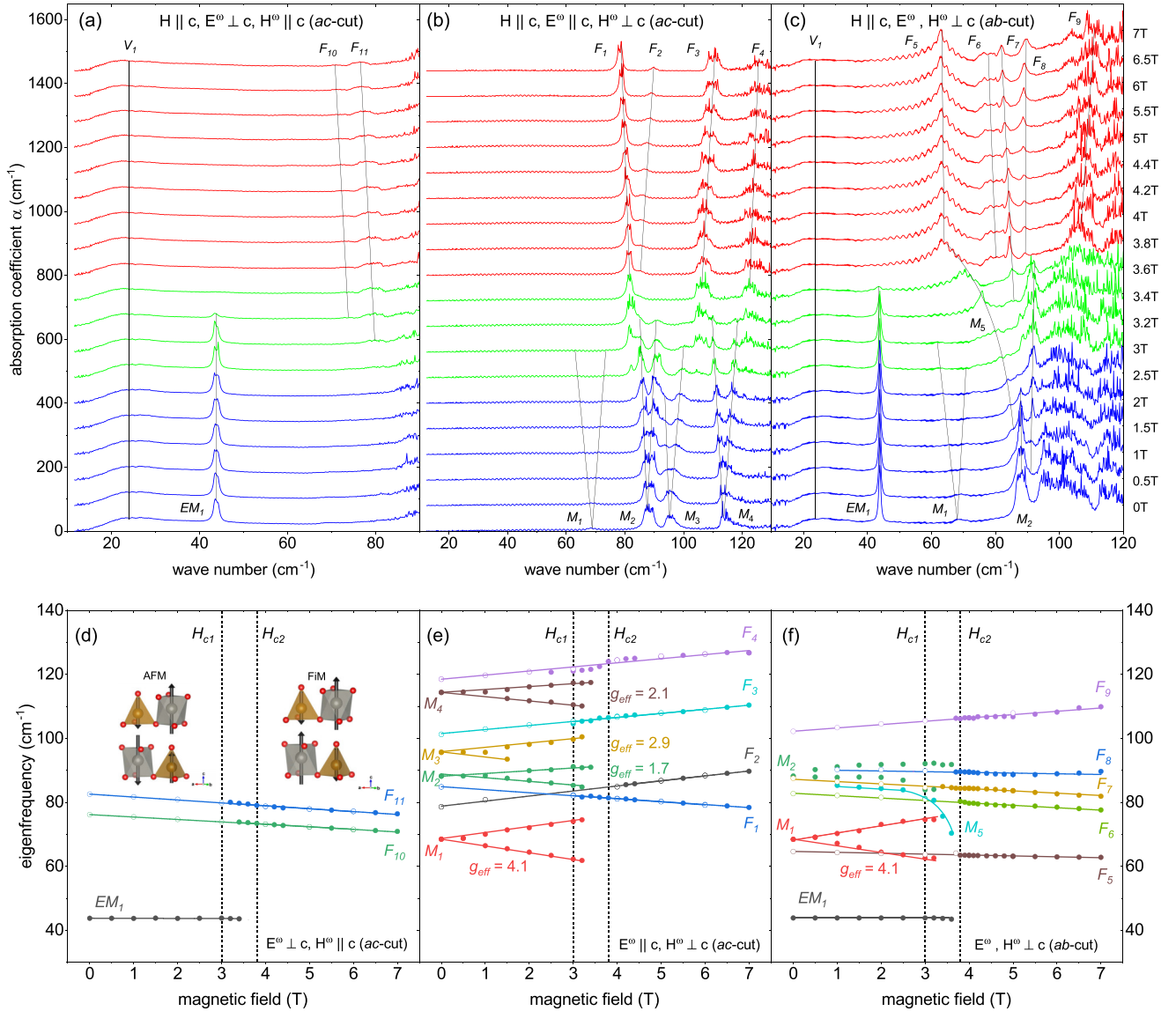


FIG. 6. Upper panels: Magnetic field dependence of the absorption spectra with  $H \parallel c$  at  $T = 13$  K in the range of 0 to 7 T for (a)  $E^\omega \perp c$ ,  $H^\omega \parallel c$  (*ac*-cut); (b)  $E^\omega \parallel c$ ,  $H^\omega \perp c$  (*ac*-cut); and (c)  $E^\omega$ ,  $H^\omega \perp c$  (*ab*-cut). All spectra are shown with a constant offset of  $80 \text{ cm}^{-1}$  with respect to the 0 T spectra. Spectra in the AFM phase are plotted in blue, for  $H_{c1} < H < H_{c2}$  in green, and in the ferrimagnetic phase in red. The solid lines are drawn to guide the eyes. Lower panels: Magnetic field dependence of the eigenfrequencies for all detected modes (except  $A_1$ ) for (d)  $E^\omega \perp c$ ,  $H^\omega \parallel c$  (*ac*-cut); (e)  $E^\omega \parallel c$ ,  $H^\omega \perp c$  (*ac*-cut); and (f)  $E^\omega$ ,  $H^\omega \perp c$  (*ab*-cut). Solid symbols represent data obtained with increasing fields starting from 0 T, while open symbols were taken upon decreasing fields. Dotted lines represent the critical fields of the magnetic transition taken from the magnetization data. The inset in panel (d) depicts the suggested collinear spin configurations of the AFM and FiM states.

that an excitation with an eigenenergy similar to that of  $M_4$  is present also in pure  $\text{Fe}_2\text{Mo}_3\text{O}_8$  and may be described as an intrinsic mode of  $\text{Fe}_2\text{Mo}_3\text{O}_8$ . Under these assumptions, we conclude that at least the three modes  $EM_1$ ,  $M_2$ , and  $M_4$  are to be regarded inherent to the magnetic structure of the pure compound, and the two doubly degenerate modes  $M_1$  and  $M_3$  may emerge due to the dilution of the magnetic iron sites by nonmagnetic zinc. Since mode  $M_5$  shifts to lower eigenfrequencies with increasing magnetic field and disappears above  $H_{c2}$ , its behavior may be interpreted as a soft mode of the magnetic phase transition. However, its relation to  $M_2$ , from where it seems to originate, remains unresolved at present.

Besides the influence of different Fe sites, the large number of magnetic modes may also be due to additional spin-stretching modes [25,26].

## B. Modes of the ferrimagnetic phase

At present we identify eleven modes,  $F_1$ – $F_{11}$ , in the spectra of the FiM phase for all measured polarization configurations above  $H_{c2}$  (see Table II). In principle, this corresponds to the number of excitation branches in the AFM phase below  $H_{c1}$ , if the  $EM_1$  mode is assumed to be doubly degenerate and  $M_5$  corresponds to a single mode.

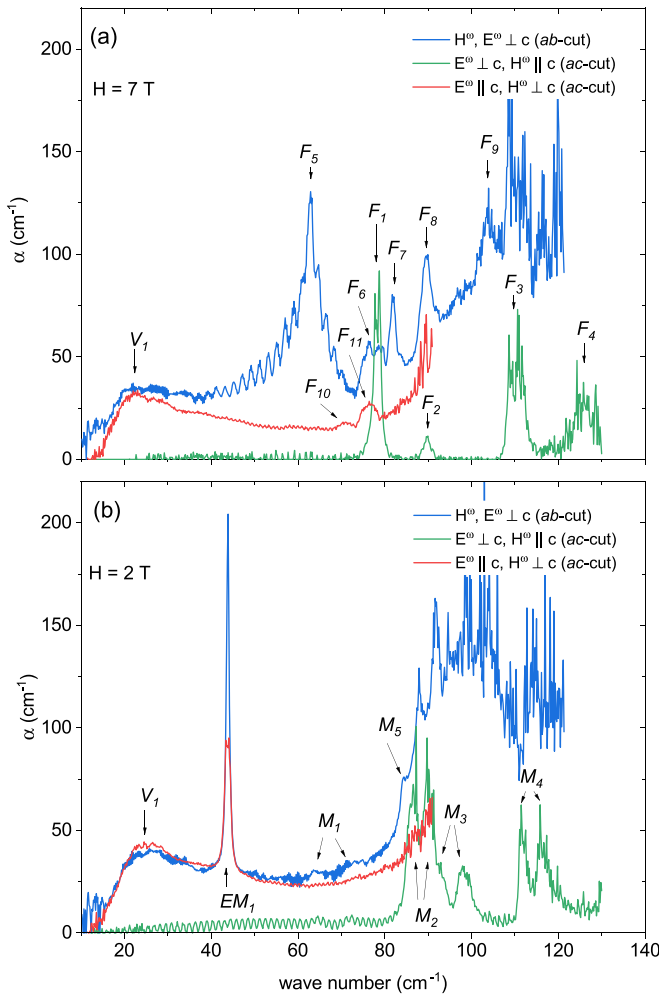


FIG. 7. Comparison of the absorption spectra (a) at  $H = 7$  T in the FiM state and (b) at  $H = 2$  T in the AFM state for the three polarization configurations. The splitting of the AFM modes  $M_1$ – $M_4$  is indicated in panel (b).

A direct comparison of the eigenfrequencies in zero field and the effective  $g$  factors estimated by  $\hbar\omega = \hbar\omega_0 + g_{\text{eff}}\mu_B H$  is provided in Table II, together with the FiM modes previously reported for  $(\text{Fe}_{1-y}\text{Zn}_y)_2\text{Mo}_3\text{O}_8$  [14–16]. The corresponding effective  $g$  factors of these modes were determined by us using the published data.

To estimate the influence of demagnetizing fields for the investigated samples we model the samples as ellipsoids [27]. The  $ab$ -cut sample is assumed to have semiaxes  $a$ ,  $b$ , and  $c$  corresponding to its approximate dimensions  $2 \times 1.5 \times 0.6$  cm<sup>3</sup> and experiences a demagnetization factor  $N_z = 0.623$  along the  $c$  axis. The  $ac$ -cut sample with  $2 \times 1.6 \times 1.48$  cm<sup>3</sup> yields  $N_z = 0.343$ . The resulting demagnetization fields  $\mu_0 N_z M_S$ , where  $M_S \simeq 0.85 \mu_B/\text{f.u.}$  denotes the magnetization value measured at 13 K in a field of 5 T as shown in Fig. 3(b), correspond then to 0.05 and 0.03 T for the  $ab$ -cut and  $ac$ -cut samples, respectively. Since the resulting fields are about 2 orders of magnitude smaller than the applied external fields in the FiM state, we neglect demagnetization effects in the following.

Unfortunately, it is not possible to determine clear selection rules for the FiM modes, either because the excitations could not be resolved experimentally or because their presence or absence in the three polarization configuration does not yield a consistent selection rule. For example, mode  $F_1$  agrees well in both eigenfrequency and  $g$  factor with the magnetic-dipole active mode  $MM_2$  reported for  $y = 0$  and  $y = 0.125$  [14], where the selection rule  $H^\omega \perp c$  was established by investigating an  $ac$ -cut sample in the Voigt configuration only. From our measurement in the Voigt configuration alone, we would derive the same selection rule, but the absence of this mode in our  $ab$ -cut measurements with  $H^\omega \perp c$  does not allow one to establish this selection rule. Similarly, modes  $F_5$ – $F_9$  should appear in one of the configurations in the  $ac$ -cut measurements to establish a selection rule, but there seem to be no corresponding excitations.

In principle, the symmetry of the FiM phase was found to allow the occurrence of gyrotropic birefringence as reported for excitations  $\nu_2$  and  $\nu_3$  for Zn concentrations of  $y = 0.25$  and  $y = 0.4$  [15], which seem to have no direct correspondence to the mode observed in this study. However, we cannot exclude that similar magnetoelectric effects might be present for some of these modes.

### C. Modeling the absorption band $V_1$ in terms of a vibronic mode

In the following we analyze the nature of the electric-dipole active excitation band  $V_1$ , which emerges and gains intensity with decreasing temperatures below  $T_N$  [see Fig. 8(b)]. It can only be observed for  $E^\omega \parallel a$  and does not exhibit any changes in magnetic fields up to 7 T. The onset of the excitation occurs at about 10 cm<sup>-1</sup>, which is in agreement with the reported energy difference between the ground and first excited state of the  $\text{Fe}^{2+}$  ions in a tetrahedral environment for pure  $\text{Fe}_2\text{Mo}_3\text{O}_8$  [11].

Strong absorption features related to transitions within the low-lying electronic  $d$ - $d$  levels of  $\text{Fe}^{2+}$  ions in tetrahedral sites have been reported for diluted  $\text{Fe}^{2+}$  on tetrahedral sites in semiconductors [28] and also in several compounds with concentrated  $\text{Fe}^{2+}$  ions, e.g., in the spinels  $\text{FeSc}_2\text{S}_4$  [29,30] and  $\text{FeCr}_2\text{S}_4$  [31] or in the system  $\text{Sr}_2\text{FeSi}_2\text{O}_7$  [32]. Moreover, electron-phonon coupling can lead to vibronic excitations, where electronic and vibrational degrees of freedom cannot be separated. In particular, the fact that the electronic eigenfrequencies of the tetrahedrally coordinated  $\text{Fe}^{2+}$  ions are of the same order of magnitude as possible involved phonon modes may foster vibronic effects [33–36]. A corresponding analysis of such low-lying vibronic excitations has been elaborated, e.g., by Testelin and coworkers [28].

Here, we follow this line and concentrate on modeling the line shape of the absorption by using the general approach to describe vibronic excitations in the case of a linear electron-phonon coupling [37,38]. The normalized absorption spectrum at  $T = 0$  can be described by

$$I(\omega) = \int_{-\infty}^{\infty} f(t)e^{i\omega t} dt \quad (1)$$

with the generating function

$$f(t) = \exp[-i\omega_0 t - S + S(t)], \quad (2)$$

TABLE II. Selection rules for the excitations  $F_1$ – $F_{11}$  found for the different polarization configurations at 13 K as shown in Fig. 5. The eigenfrequencies  $\omega_0$  correspond to the zero-field values in the FiM phase. The sign of  $g_{\text{eff}}$  indicates the sign of the linear slope with increasing magnetic field. The notations  $\checkmark$  and  $\times$  indicate the presence or absence of a mode. The cases when no observation was possible are denoted as n.r. (not resolved). The lower part of the table lists reported modes of the FiM phase for different Zn concentrations and their assigned optical activity taken from Refs. [14–16].

Mode	$\omega_0$ ( $H^{\text{dc}} = 0$ T) ( $\text{cm}^{-1}$ )	$g_{\text{eff}}$	<i>ab</i> -cut		<i>ac</i> -cut		Activity
			$E^\omega, H^\omega \perp c$	$E^\omega \perp c, H^\omega \parallel c$	$E^\omega \parallel c, H^\omega \perp c$		
$F_1$	85	−2.0	$\times$	$\times$	$\checkmark$		?
$F_2$	79	3.4	$\times$	$\times$	$\checkmark$		?
$F_3$	102	2.7	$\times$	n.r.	$\checkmark$		?
$F_4$	119	2.7	n.r.	n.r.	$\checkmark$		?
$F_5$	65	−0.6	$\checkmark$	$\times$	$\times$		?
$F_6$	83	−1.6	$\checkmark$	$\times$	$\times$		?
$F_7$	87	−1.7	$\checkmark$	$\times$	$\times$		?
$F_8$	91	−0.2	$\checkmark$	n.r.	$\times$		?
$F_9$	102	2.3	$\checkmark$	n.r.	$\times$		?
$F_{10}$	76	−1.7	$\times$	$\checkmark$	$\times$		?
$F_{11}$	83	−1.9	$\times$	$\checkmark$	$\times$		?
<i>MM2</i> ( $y = 0$ )	87	−2.0	–	$\times$	$\checkmark$		$H^\omega \perp c$
<i>MM2</i> , $v_3$ ( $y = 0.125$ )	87	−2.5	–	$\times$	$\checkmark$		$H^\omega \perp c$
$v_1$ ( $y = 0.25$ )	47	4.0	–	$\times$	$\checkmark$		$H^\omega \perp c$
$v_2$ ( $y = 0.25$ )	76	2.6	–	$\times$	$\checkmark$		$H^\omega \perp c$
$v_3$ ( $y = 0.25$ )	87	−2.6	–	$\checkmark$	$\checkmark$		$E^\omega, H^\omega \perp c$
$v_1$ ( $y = 0.4$ )	47	4.0	–	$\checkmark$	$\checkmark$		$E^\omega, H^\omega \perp c$
$v_2$ ( $y = 0.4$ )	73	3.6	–	$\times$	$\checkmark$		$H^\omega \perp c$
$v_3$ ( $y = 0.4$ )	87	−3.1	–	$\checkmark$	$\checkmark$		$E^\omega, H^\omega \perp c$
$v_4$ ( $y = 0.5$ )	42	–	–	$\times$	$\checkmark$		$H^\omega \perp c$

where

$$S(t) = \int_0^\infty s(\omega) e^{-i\omega t} d\omega \quad (3)$$

is determined by the coupling function  $s(\omega)$ , which describes the distribution of phonon modes in a given material and  $S = S(t = 0)$ . Expanding  $f(t)$  in a power series in  $S(t)$  results in

$$I(\omega) = e^{-S} \sum_{n=0}^{\infty} \frac{S^n}{n!} \Gamma_n(\omega), \quad (4)$$

with

$$\Gamma_n(\omega) = \int_{-\infty}^{\infty} e^{i(\omega - \omega_0)t} \left[ \frac{S(t)}{S} \right]^n dt, \quad (5)$$

which can be calculated iteratively for  $n > 1$  by the convolution

$$\Gamma_n(\omega) = \int_{-\infty}^{\infty} \Gamma_{n-1}(\omega') \Gamma_1(\omega + \omega_0 - \omega') d\omega'. \quad (6)$$

The number  $n$  corresponds to the number of phonons involved in the absorption process [37] and, hence, the zero-phonon line with  $n = 0$  describes the purely electronic transition at  $\omega_0$ , which is not visible in our spectra.

In order to simulate the vibrational line shape the choice of a suitable coupling function is important. Optically active phonons are usually at frequencies higher than that of the observed absorption band, and therefore, we consider a coupling to acoustic phonons, which are usually modeled by a Debye-like phonon density of states. Using an exponential decay around the Debye frequency  $\omega_1$  instead of a sharp cutoff

[39] leads to the first term in our coupling function

$$s(\omega) = \exp\left(-\frac{\omega}{\omega_1}\right) \frac{\omega^2 S_1}{2\omega_1^3} + \exp\left(-\frac{\omega}{\omega_2}\right) \frac{\omega^3 S_2}{6\omega_2^4}. \quad (7)$$

This first Debye-like term alone, however, does not allow one to fully capture the entire absorption band. Therefore, the second term with a cutoff frequency of  $\omega_2$  is introduced as an empirical modification of the phonon density of states, satisfying the condition  $S = S_1 + S_2$  as required [38]. Note that this second term was suggested to model molecular vibronic spectra with the same approach used here [40]. The choice of the second term is somewhat arbitrary and other terms satisfying  $S = S_1 + S_2$  might give the same result. As the experimental phonon density of states is not available for comparison with the coupling function, this term and its additional two parameters are deemed, however, necessary to describe the entire absorption curve successfully as we discuss in the following.

In order to analyze the line shape of the  $V_1$  excitation, we use a spectrum obtained for  $E^\omega \perp c, H^\omega \perp c$  (*ab*-cut sample) and subtract the high-frequency contribution stemming from the lowest-lying infrared-active phonon modeled by a Lorentzian line shape with eigenfrequency  $\omega_0 = 128.6 \text{ cm}^{-1}$ , damping  $\gamma = 9.0 \text{ cm}^{-1}$ , and ionic plasma frequency  $\omega_p = 158.4 \text{ cm}^{-1}$  [see Fig. 8(a)] in agreement with reported data for pure  $\text{Fe}_2\text{Mo}_3\text{O}_8$  [22]. As the narrow electric-dipole excitation  $EM_1$  on top of the  $V_1$  band is suppressed in the ferrimagnetic phase above  $H_{c2}$  (see Fig. 6) and  $M_1$  is clearly magnetic in origin, while  $V_1$  does not alter, we do not consider any coupling of these excitations.



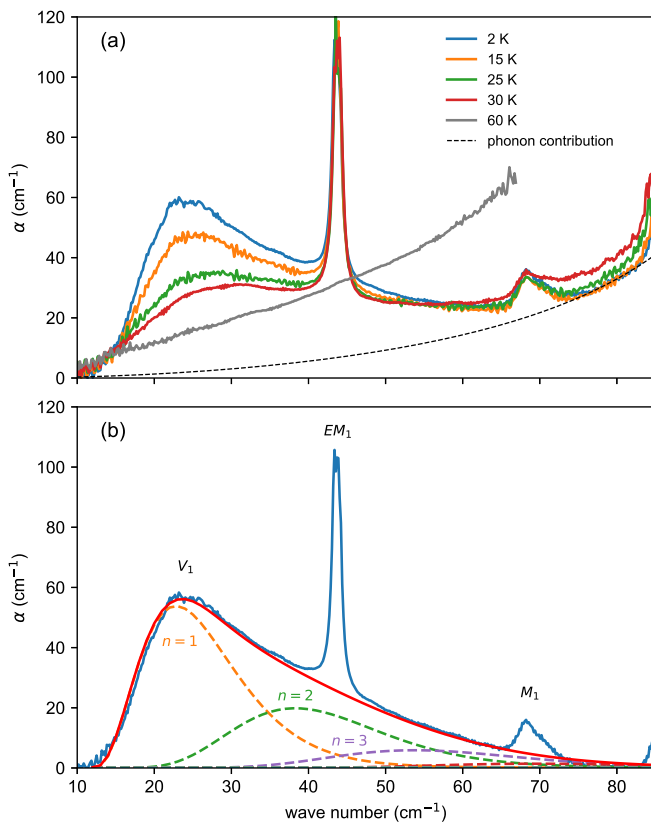


FIG. 8. (a) THz absorption data at various temperatures for  $E^\omega \perp c$ ,  $H^\omega \perp c$ , and a Lorentzian phonon contribution of the lowest-lying phonon as described in the text (black dashed line). (b) THz absorption spectrum at 2 K, where the phonon contribution was subtracted, and a simulation using Eqs. (4) and (7), including the contributions for  $n = 1, 2$ , and  $3$  (dashed lines).

To restrict the parameters for this simulation, we fixed the zero-phonon line to  $\omega_0 = 12 \text{ cm}^{-1}$ , a value close to experimental [22,23] and theoretical estimates [11] and minimized the number of phonons involved in the process to  $n = 3$ . Using these constraints, we could reproduce the experimental line shape with the five parameters  $S_1 = 0.02$ ,  $S_2 = 1.1$ ,  $\omega_1 = 12 \text{ cm}^{-1}$ ,  $\omega_2 = 3.6 \text{ cm}^{-1}$ , and the amplitude  $A = 2.4 \times 10^3 \text{ cm}^{-1}$ , which is defined by  $\alpha(\omega) = AI(\omega)$ . The agreement between data and simulation is very good and, hence, we conclude that this simple approach satisfactorily reproduces the  $V_1$  band and supports a vibronic origin of the band. Note, that higher convolutions for  $n > 3$  do only weakly modify the high-frequency tail. The values for  $\omega_1$  and  $\omega_2$  must be

regarded as a parametrization of the acoustic phonon branches coupled to the electronic transitions. As such a vibronic band has not been reported for pure  $\text{Fe}_2\text{Mo}_3\text{O}_8$  [14], we assume that the disorder introduced by the Zn ions and the corresponding impurity modes are responsible for the occurrence of this absorption band. It remains to be clarified why THz studies of comparable samples with  $y > 0$  do not report a similar feature [14–16] and why this mode can only be observed below  $T_N$ .

A possible explanation for the emergence below  $T_N$  could be that long-range magnetic ordering triggers the splitting of the lowest-lying iron orbitals as suggested in Ref. [11]. Moreover, some of us recently reported the emergence of electronic excitations in the far- and mid-infrared regime related to the higher-lying  $d-d$  transition of the  $\text{Fe}^{2+}$  ions at tetrahedral sites in pure  $\text{Fe}_2\text{Mo}_3\text{O}_8$  below  $T_N$ , where energy scales of 13 and 26  $\text{cm}^{-1}$  occur as a difference between the observed transitions. This corroborates our interpretation that the vibronic band involves the lowest-lying electronic states of  $\text{Fe}^{2+}$  ions at tetrahedral sites.

## VI. SUMMARY

We observed 10 magnetic modes in the AFM state in  $\text{Fe}_{1.86}\text{Zn}_{0.14}\text{Mo}_3\text{O}_8$  in finite magnetic fields, including both magnetic- and electric-dipole active modes. Assuming that the lowest-lying mode is a doublet with an unresolved splitting in the magnetic fields applied in this study, the actual number of AFM modes would increase to 11. This is the number of modes observed in the magnetic-field-induced FiM state in  $\text{Fe}_{1.86}\text{Zn}_{0.14}\text{Mo}_3\text{O}_8$ . The large number of modes, far exceeding the number of magnetic sublattices in pure  $\text{Fe}_2\text{Mo}_3\text{O}_8$ , may imply that the number of magnetic sublattices is increased due to Zn substitution on the tetrahedral sites. Another possible reason for the large number of excitations is that spin-stretching modes also become optically active, besides the precessional modes described by linear spin-wave theory. In the transition region between the two magnetic phases a coexistence of AFM and FiM modes is present, implying a coexistence of AFM and FiM phases for  $H_{c1} < H < H_{c2}$ . Additionally, a broad electric-dipole active excitation band was observed in the AFM phase and our analysis strongly suggests that it is of vibronic origin involving the lowest-lying electronic  $d$  states of Fe in tetrahedral environment, which are split by about  $12 \text{ cm}^{-1}$ .

## ACKNOWLEDGMENTS

We acknowledge support by the Deutsche Forschungsgemeinschaft via TRR 80 (Project No. 107745057) and by the project ANCD No. 20.80009.5007.19 (Moldova).

- [1] N. A. Spaldin and R. Ramesh, *Nat. Mater.* **18**, 203 (2019).  
 [2] S. Dong, H. Xiang, and E. Dagotto, *Nat. Sci. Rev.* **6**, 629 (2019).  
 [3] I. Kézsmárki, U. Nagel, S. Bordács, R. S. Fishman, J. H. Lee, H. T. Yi, S. W. Cheong, and T. Rődm, *Phys. Rev. Lett.* **115**, 127203 (2015).

- [4] T. Jungwirth, J. Sinova, A. Manchon, X. Marti, J. Wunderlich, and C. Felsler, *Nat. Phys.* **14**, 200 (2018).  
 [5] V. Baltz, A. Manchon, M. Tsoi, T. Moriyama, T. Ono, and Y. Tserkovnyak, *Rev. Mod. Phys.* **90**, 015005 (2018).  
 [6] A. Sasaki, S. Yui, and M. Yamaguchi, *Mineral. J.* **12**, 393 (1985).

- [7] D. Bertrand and H. Kerner-Czeskleba, *J. Phys.* **36**, 379 (1975).
- [8] W. H. McCarroll, L. Katz, and R. Ward, *J. Am. Chem. Soc.* **79**, 5410 (1957).
- [9] S. P. McAlister and P. Strobel, *J. Magn. Magn. Mater.* **30**, 340 (1983).
- [10] Y. Wang, G. L. Pascut, B. Gao, T. A. Tyson, K. Haule, V. Kiryukhin, and S.-W. Cheong, *Sci. Rep.* **5**, 12268 (2015).
- [11] F. Varret, H. Kerner-Czeskleba, F. Hartmann-Boutron, and P. Imbert, *J. Phys. France* **33**, 549 (1972).
- [12] F. A. Cotton, *Inorg. Chem.* **3**, 1217 (1964).
- [13] T. Kurumaji, S. Ishiwata, and Y. Tokura, *Phys. Rev. X* **5**, 031034 (2015).
- [14] T. Kurumaji, Y. Takahashi, J. Fujioka, R. Masuda, H. Shishikura, S. Ishiwata, and Y. Tokura, *Phys. Rev. B* **95**, 020405(R) (2017).
- [15] T. Kurumaji, Y. Takahashi, J. Fujioka, R. Masuda, H. Shishikura, S. Ishiwata, and Y. Tokura, *Phys. Rev. Lett.* **119**, 077206 (2017).
- [16] S. Yu, B. Gao, J. W. Kim, S. W. Cheong, M. K. L. Man, J. Madeo, K. M. Dani, and D. Talbayev, *Phys. Rev. Lett.* **120**, 037601 (2018).
- [17] I. V. Solovyev and S. V. Streltsov, *Phys. Rev. Mater.* **3**, 114402 (2019).
- [18] S. Nakayama, R. Nakamura, and M. Akaki, *J. Phys. Soc. Jpn.* **80**, 104706 (2011).
- [19] S. V. Streltsov, D.-J. Huang, I. Solovyev, and D. I. Khomskii, *JETP Lett.* **109**, 786 (2019).
- [20] J. Bertinshaw, C. Ulrich, A. Günther, F. Schrettle, M. Wohlaue, S. Krohns, M. Reehuis, A. J. Studer, M. Avdeev, D. V. Quach, J. R. Groza, V. Tsurkan, A. Loidl, and J. Deisenhofer, *Sci. Rep.* **4**, 6079 (2014).
- [21] A. Abragam and B. Bleaney, *Electron Paramagnetic Resonance of Transition Ions* (Oxford University, Oxford, 1970).
- [22] S. Reschke, A. A. Tsirlin, N. Khan, L. Prodan, V. Tsurkan, I. Kézsmárki, and J. Deisenhofer, *Phys. Rev. B* **102**, 094307 (2020).
- [23] T. N. Stanislavchuk, G. L. Pascut, A. P. Litvinchuk, Z. Liu, S. Choi, M. J. Gutmann, B. Gao, K. Haule, V. Kiryukhin, S. W. Cheong, and A. A. Sirenko, *Phys. Rev. B* **102**, 115139 (2020).
- [24] A. Strinic *et al.* (unpublished).
- [25] K. Penc, J. Romhányi, T. Rößm, U. Nagel, A. Antal, T. Fehér, A. Jánossy, H. Engelkamp, H. Murakawa, Y. Tokura, D. Szaller, S. Bordács, and I. Kézsmárki, *Phys. Rev. Lett.* **108**, 257203 (2012).
- [26] V. Kocsis, K. Penc, T. Rößm, U. Nagel, J. Vít, J. Romhányi, Y. Tokunaga, Y. Taguchi, Y. Tokura, I. Kézsmárki, and S. Bordács, *Phys. Rev. Lett.* **121**, 057601 (2018).
- [27] J. A. Osborn, *Phys. Rev.* **67**, 351 (1945).
- [28] C. Testelin, C. Rigaux, A. Mauger, A. Mycielski, and C. Julien, *Phys. Rev. B* **46**, 2183 (1992).
- [29] L. Mittelstädt, M. Schmidt, Z. Wang, F. Mayr, V. Tsurkan, P. Lunkenheimer, D. Ish, L. Balents, J. Deisenhofer, and A. Loidl, *Phys. Rev. B* **91**, 125112 (2015).
- [30] N. J. Laurita, J. Deisenhofer, L. D. Pan, C. M. Morris, M. Schmidt, M. Johnsson, V. Tsurkan, A. Loidl, and N. P. Armitage, *Phys. Rev. Lett.* **114**, 207201 (2015).
- [31] A. Strinic, S. Reschke, K. V. Vasin, M. Schmidt, A. Loidl, V. Tsurkan, M. V. Eremin, and J. Deisenhofer, *Phys. Rev. B* **102**, 134409 (2020).
- [32] T. T. Mai, C. Svoboda, M. T. Warren, T.-H. Jang, J. Brangham, Y. H. Jeong, S.-W. Cheong, and R. Valdes Aguilar, *Phys. Rev. B* **94**, 224416 (2016).
- [33] J. T. Vallin, *Phys. Rev. B* **2**, 2390 (1970).
- [34] E. E. Vogel and J. Rivera-Iratchet, *Phys. Rev. B* **22**, 4511 (1980).
- [35] S. Wittekoek, R. P. Van Staple, and A. W. Wijma, *Phys. Rev. B* **7**, 1667 (1973).
- [36] L. F. Feiner, *J. Phys. C: Solid State Phys.* **15**, 1515 (1982).
- [37] A. M. Stoneham, *Theory of Defects in Solids* (Oxford University, Oxford, 1975).
- [38] Y. Toyozawa, *Optical Processes in Solids* (Cambridge University, New York, 2003).
- [39] T. Pullerits, R. Monshouwer, F. van Mourik, and R. van Grondelle, *Chem. Phys.* **194**, 395 (1995).
- [40] M. Rätsep, M. Pajusalu, J. M. Linnanto, and A. Freiberg, *J. Chem. Phys.* **141**, 155102 (2014).